

Autonomous Dissection in Robotic Cholecystectomy

Ki-Hwan Oh¹, Leonardo Borgioli¹, Miloš Žefran¹, Valentina Valle² and Pier Cristoforo Giulianotti²

Abstract—Robotic surgery offers enhanced precision and adaptability, paving the way for automation in surgical interventions. Cholecystectomy, the gallbladder removal, is particularly well-suited for automation due to its standardized procedural steps and distinct anatomical boundaries. A key challenge in automating this procedure is dissecting with accuracy and adaptability. This paper presents a vision-based autonomous robotic dissection architecture that integrates real-time segmentation, keypoint detection, grasping and stretching the gallbladder with the left arm, and dissecting with the other. We introduce an improved segmentation dataset based on videos of robotic cholecystectomy performed by various surgeons, incorporating a new “liver bed” class to enhance boundary tracking after multiple rounds of dissection. Our system employs state-of-the-art segmentation models and an adaptive boundary extraction method that maintains accuracy despite tissue deformations and visual variations. Moreover, we implemented an automated grasping and pulling strategy to optimize tissue tension before dissection upon our previous work. Ex vivo evaluations on porcine livers demonstrate that our framework significantly improves dissection precision and consistency, marking a step toward fully autonomous robotic cholecystectomy.

I. INTRODUCTION

Robotic-assisted surgery (RAS) continues revolutionizing modern medicine by enabling higher precision, reduced patient trauma, and faster recovery than traditional open or laparoscopic procedures. This favorable setting has spurred research into automating various surgical tasks such as tissue ablation [1], blunt dissection [2], [3], and suturing [4]–[9]. For instance, the work in [10] demonstrated an algorithm for automated suturing based on visual tracking. At the same time, point cloud-based methods have been explored to model soft tissue deformations [2], estimate applied forces [11], [12], and for surgical planning [13].

Most prior approaches to task automation in RAS rely on endoscopic imaging, which poses challenges due to its two-dimensional representation and variable lighting conditions. Advanced segmentation and detection techniques are critical for overcoming these limitations. Recent breakthroughs brings new frameworks for subtask automations [14], with for example endoscopic servo control [15]. However, their methods often remain confined to pixel-level processing without establishing logical tissue connections [16], or relying on markers [17].

Among various interventions, cholecystectomy, the surgical removal of the gallbladder attached to the liver, has emerged as an ideal testbed for automation due to its relatively straightforward anatomy and standardized sequence of surgical steps. Previously [18], we introduced a framework to automate the control of a single da Vinci surgical robot instrument relying only on endoscopic images, like surgeons, to dissect¹ along the trajectory between the porcine gallbladder and the liver. However, we faced some limitations: (a) the dataset we generated was preliminary, and thus, the trained model could not perform as expected under varying conditions, such as changes in tissue colors over time and variations in the size and shape of the gallbladder; and (b) the dissection trajectory was planned offline, but we discovered that the tissue deformed after the energy was applied even though the tissues were not touched with other instruments.

To address these shortcomings, we present a new segmentation dataset based on the Comprehensive Robotic Cholecystectomy Dataset (CRCDD) [19], [20], which includes robotic cholecystectomy procedures performed with the classic da Vinci system. In addition, we introduce a new class for tissue segmentation that corresponds to the region where the gallbladder used to be attached to the liver (*liver bed*) so the model can track the boundary even after multiple rounds of dissection. Furthermore, we train several state-of-the-art models for tissue instance segmentation, such as the MaskDINO [21] and YOLO11 [22], and compare the performance with the previous Detectron2 [23] model. We also develop an online boundary extraction method and an improved method for following the boundary. Finally, we propose a novel method to automatically grasp and pull the tissue before dissection. Together, the ability to track the boundary online and grasp the gallbladder represents a major step towards making our automated procedure much closer to how surgeons perform dissection. The effectiveness of our framework is successfully evaluated ex-vivo using porcine liver.

Our contributions are twofold: (a) developing a comprehensive vision-based control framework that integrates online segmentation and keypoint detection for precise dissection along tissues that deform in time; (b) a framework that allows the robot to automatically grasp the gallbladder to maximize tissue tension and dissect the gallbladder from the liver, adapting to tissue deformations; and (c) an ex vivo evaluation that demonstrates the performance of the system in a realistic surgical scenario.

¹In the surgical literature, dissection refers to the actual separation of tissues; in our work, the term refers to energy delivery to a particular location on a specimen.

*This work was not supported by any organization

¹K.H. Oh, L. Borgioli and Miloš Žefran are with the Robotics Lab, Department of Electrical and Computer Engineering, College of Engineering, University of Illinois Chicago, Chicago, IL 60607, USA.

²V. Valle and P.C. Giulianotti are with the Surgical Innovation and Training Lab, Department of Surgery, College of Medicine, University of Illinois Chicago, Chicago, IL 60607, USA.

II. EXPANDED DATASET

A. Revised Custom Segmentation Dataset

One limitation of our previous dataset was the lack of variability in gallbladder and liver features, such as differences in shape, size, and color. Additionally, we observed that the model struggled to track deformed tissues after monopolar energy was applied via the electro-surgical unit, as the dissected region no longer resembled the original gallbladder or liver (Fig. 7). These limitations prevented the robot from performing multiple rounds of dissection, which is necessary for the complete separation of the gallbladder from the liver.

To address these challenges, we enriched the segmentation dataset by introducing a new label, liver bed, which represents the liver surface where the gallbladder was previously attached (Fig. 1). We used the Segment Anything Model 2 (SAM2) [24] to annotate videos from the Comprehensive Robotic Cholecystectomy Dataset (CRCDC) [19], [20], a large-scale ex vivo robotic cholecystectomy dataset featuring procedures performed by multiple surgeons. This dataset closely aligns with our intended application and captures the dynamic tissue variations during surgery. SAM2 segments objects in single images or sequential video frames using prompts such as pixel-based cues or bounding boxes. However, SAM2 does not inherently classify the segmented regions, so we manually labeled each tissue category to create a structured training dataset. This allowed us to fine-tune state-of-the-art instance segmentation models, including YOLO11, for improved tissue recognition.

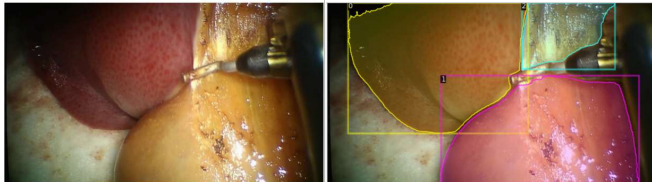


Fig. 1: Example of tissue segmentation annotation to train the model. The tissue is Liver (Orange), Gallbladder (Pink), and Liver Bed (Green)

The number of annotations of the new segmentation dataset is shown in Table I. These improvements contribute to a more robust dataset that better represents real-world surgical conditions, facilitating the development of more accurate and reliable segmentation models.

Data Type	Categories	Train instances	Test instances
Segmentation	Pig Liver	25988	8690
	Pig Gallbladder	25988	8690
	Liver Bed	21660	7261
Keypoints	FBF	5476	1372
	PCH	7320	1831

TABLE I: Description of the annotated dataset. Keypoints were annotated for the Fenestrated Bipolar Forceps (FBF) and Permanent Cautery Hook (PCH).

B. Keypoints

We also expanded the keypoint dataset to have stronger keypoint tracking of the instruments. The annotations for surgical instruments, including Fenestrated Bipolar Forceps (FBF) and Permanent Cautery Hook (PCH), were manually performed using the COCO annotator [25]. Moreover, we used a different keypoint structure for each instrument to ensure robustness against common transformations. Fig. 2 illustrates the keypoint locations of the FBF and PCH. These keypoints are strategically placed on instrument regions with distinct colors and edges to optimize detection accuracy. Table I details the number of annotated instances for the extended instrument keypoint dataset. Both the segmentation and keypoint dataset follow Microsoft’s COCO format [26], ensuring compatibility with diverse object detection models.

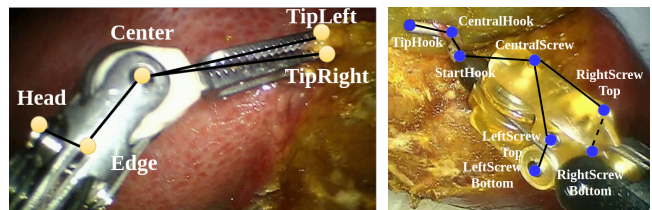


Fig. 2: Keypoints structure for each instrument. Fenestrated Bipolar Forceps (FBF, left). Permanent Cautery Hook (PCH, right).

III. METHODOLOGY

A. Hardware Setup

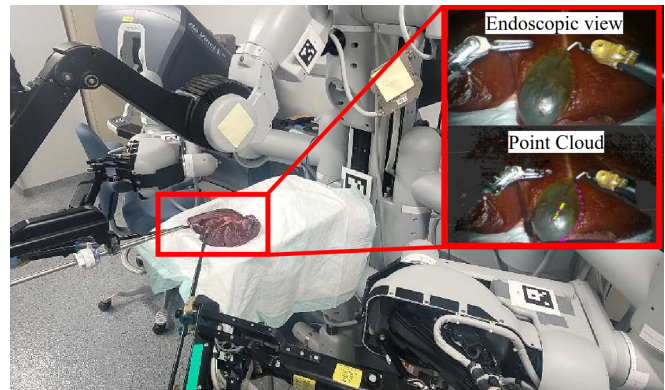


Fig. 3: The experimental setup: a porcine liver with the gallbladder attached is placed on a tray facing the ceiling. The endoscopic view and the generated point cloud from the stereo endoscope with the extracted features are shown in the top right corner.

Our system utilizes a first-generation da Vinci with the dVRK [27] and a Si model endoscope for enhanced image quality and reduced noise. To control the monopolar current from the electro-surgical unit (ESU), we interfaced the energy cables and console pedals with an Arduino UNO [20]. Additionally, we calibrated the stereo endoscope to generate 3D point clouds and performed a custom robot arm calibration to minimize dVRK errors [18] (Fig. 3). Moreover, we upgraded the implementation platform to ROS2 [28].

B. Image/Point Cloud Post-Processing

We applied the following image-processing steps to design an online version of tracking the boundary of interest and to align the FBF and PCH with the tissues for better performance. First, we used the classical skeletonization algorithm [29], which iteratively sweeps a fixed-size window over the binary mask of the object, removing pixels at each iteration until the image stops changing. Since the gallbladder has an oval-like shape, the 3D skeleton points derived from the point cloud effectively represent its medial surface (yellow points in the figures). The boundary of interest (purple points in the figures) is the interface between the liver and the gallbladder and corresponds to the points on the right side of the skeleton. By applying Principal Component Analysis (PCA) [30] to the adjacent and skeleton points, we extract the principal axis that points to the right side of the skeleton, aiding in precise boundary alignment.

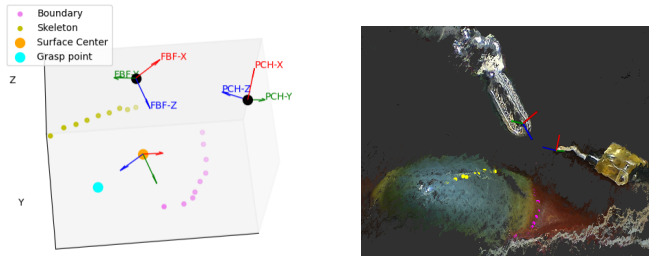


Fig. 4: The frames of each instrument and the surface between the skeleton and the boundary of the gallbladder after instrument alignment.

C. Grasping

We divided the grasping task into three steps: align, grasp, and pull. First, we align the pose of the FBF to be parallel to the surface of the gallbladder of interest, which is the region between the boundary and skeleton points obtained from the post-processing step. We apply PCA to the points surrounding this surface to determine the alignment pose. We realigned the principal axes of the gallbladder surface when necessary to ensure that the secondary axis extends from the skeleton to the boundary points and the normal axis of the surface is oriented perpendicular to the gallbladder surface, directed along the viewing direction of the endoscope. This alignment guarantees consistency in orientation across different viewpoints. The resulting three principal axes approximate a local frame attached to the right-side surface of the gallbladder. The FBF frame is oriented based on this local frame (Fig. 4). Once aligned, the FBF moves along its negative x-axis, facing through the gallbladder surface, to reach the grasping point between the center of the skeleton and the boundary, offset by a certain distance along the grasping direction. After grasping, the FBF pulls the gallbladder along its negative z-axis, tangential to the right-side surface of the gallbladder, until the boundary becomes nearly linear, where the deviation of the boundary is below 0.5mm (Fig. 5).

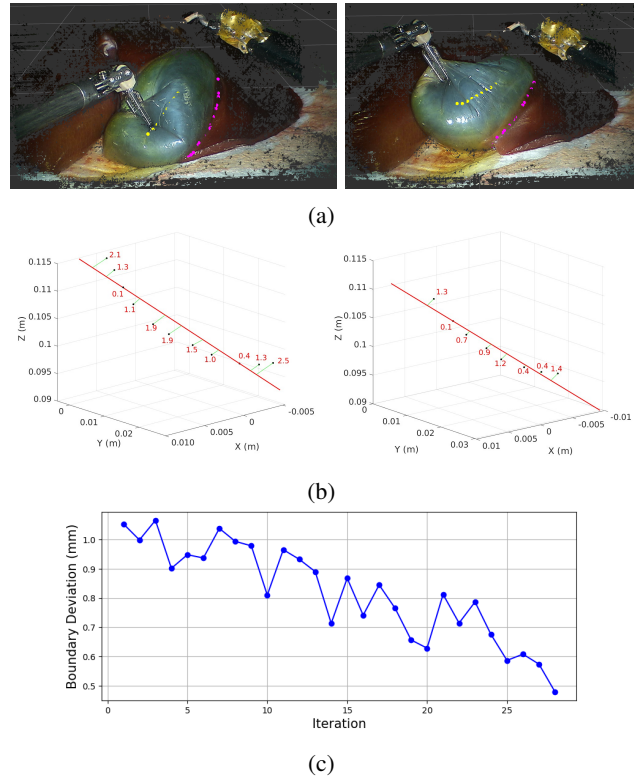


Fig. 5: (a) Before (left) and after (right) pulling the gallbladder. (b) The deviation of the boundary points to the ideal boundary (red line) before the pull (left) and after the pull (right). (c) Shows the deviation of the boundary points (purple); the lower the deviation, the closer the boundary is to a straight line.

D. Dissection

Similar to grasping, we first align the PCH to the gallbladder’s surface before performing the dissection. The alignment method is identical to grasping, except the frame axes are mapped based on the PCH’s pose rather than the FBF’s (Fig. 4). Unlike our previous approach, where the PCH followed a fixed trajectory, we now extract a target point from the online boundary. Initially, this target point is the first point of the current boundary, where boundary points are ordered clockwise from the gallbladder’s center. Once the PCH reaches the target point, the algorithm will search for the next one within the new boundary, selecting the point with the maximum distance—up to 1cm —from its current position while maintaining alignment with its movement direction. The round of the dissection will terminate when finding a target point sufficiently far (over 1mm) from the current PCH location is impossible.

IV. EXPERIMENTAL RESULTS

A. Instrument Keypoint Detection

Detectron2 [23] offers two independent model types: instance object segmentation and keypoint detection. To avoid confusion, we refer to these models as DT2-seg and DT2-kpt. For keypoint prediction with YOLO11, we selected

YOLO11l-pose, which delivers performance comparable to its largest variant (YOLO11x-pose) while offering twice the inference speed [22].

Model	Categories	AP (Bbox.)	AP (Kpt.)
DT2-kpt	FBF	77.1	94.6
	PCH	74.2	98.4
YOLO11l-pose	FBF	66.8	97.2
	PCH	85.4	98.6

TABLE II: The Average Precision (AP) scores for instrument keypoints detection.

Table II presents the results of the fine-tuned keypoint detection models. The Average Precision (AP) scores used in this paper are the mAP50-95² [26], which provide a comprehensive view of the model’s performance across different levels of detection difficulty. The scores demonstrate that YOLO11l-pose outperforms DT2-kpt. Additionally, Fig. 6 provides a qualitative comparison, highlighting YOLO11l-pose’s improved keypoint localization, particularly in cases where keypoints are partially obscured or near the image frame’s edges. These enhancements are crucial in practical applications where occlusion occurs and make keypoint detection accuracy challenging.

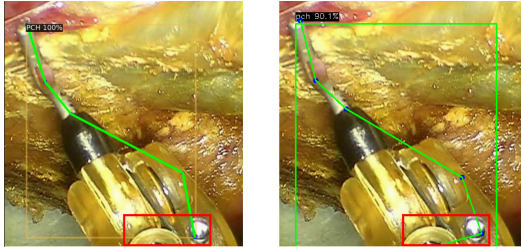


Fig. 6: Keypoints prediction for DT2-kpt (left) and YOLO11l-pose (right), this example shows some limitations of the DT2-kpt to detect some keypoints when the tool is on the edges of the image (red rectangle).

B. Tissue Instance Segmentation

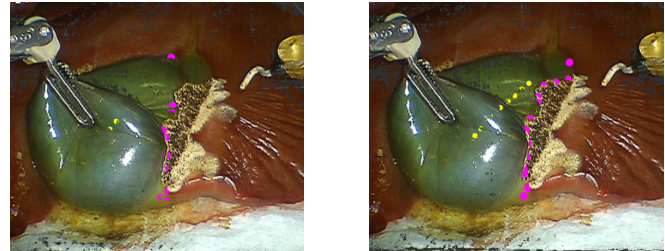
Model	Categories	AP (Bbox.)	AP (Seg.)
DT2-seg	Liver	61.2	83.9
	Gallbladder	96.2	89.8
	Liver Bed	91.1	75.3
MaskDINO	Liver	55.3	80.0
	Gallbladder	96.7	99.0
	Liver Bed	88.9	91.3
YOLO11l-seg	Liver	99.3	98.6
	Gallbladder	99.5	97.7
	Liver Bed	99.2	93.0

TABLE III: The Average Precision (AP) scores for each category (Bbox. stands for Bounding box and Seg. for Segmentation).

Table III presents the AP scores for each model fine-tuned on our new segmentation dataset. The results indicate that segmentation AP scores are more consistent across models,

²the average of the mean average precision calculated at varying intersection over union (IoU) thresholds, ranging from 0.50 to 0.95

suggesting that the new dataset is more comprehensive than our previous one [20]. While MaskDINO achieved the highest precision in detecting the gallbladder, YOLO11l-seg outperformed both MaskDINO and DT2-seg in overall performance.



(a) DT2-seg (Old) [18]

(b) YOLO11

Fig. 7: Comparing the performance between (a) the model we used in our previous work and (b) the recent YOLO11 on detecting the bounding after a few rounds of dissection.

Both DT2-seg and MaskDINO struggled with detecting the *liver*, likely due to its similarity to the *liver bed*, which is part of the liver’s surface layer. In contrast, YOLO11l-seg demonstrated the ability to differentiate between these two tissues, as reflected in its AP scores. The limitations of DT2-seg and MaskDINO may not be critical during the initial stages of dissection when the liver bed is not yet exposed. However, their reduced accuracy could impact performance in later stages, particularly after the liver has cauterization marks.

Nevertheless, Fig. 7 highlights the necessity of the new class and its impact on boundary determination after multiple rounds of dissection to advance towards actual robotic cholecystectomy. In Fig 7a, the previous model’s estimations show a disconnected boundary and difficulties detecting the full gallbladder, displaying an incomplete skeleton. In contrast, Fig. 7b demonstrates the improved model’s ability to accurately detect the boundary and the entire gallbladder with a complete skeleton.

C. Procedure Performance

Fig. 4 and Fig. 5 illustrate the stages of gallbladder grasping. The success of the grasping phase does not heavily depend on the models used; instead, the primary objective is to ensure that the boundary is sufficiently stretched for dissection and that the FBF remains stable throughout the procedure. Consequently, our focus is primarily on evaluating the dissection performance after the gallbladder has been adequately stretched, allowing for a direct comparison with results from our previous work. The FBF was not repositioned after the initial grasping to ensure consistency across trials. For Detectron2, we used DT2-seg and DT2-kpt to maintain the previous experimental setup, with both models fine-tuned on the new dataset. We then compared their performance with both our prior results and state-of-the-art models.

Fig. 8 presents the recorded boundary points from one of the trials, comparing YOLO11l to DT2, demonstrating that the YOLO’s boundary remained stable over time. The results

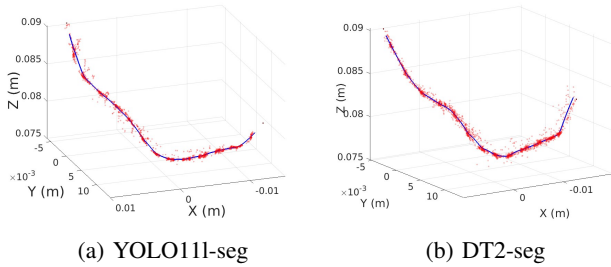


Fig. 8: Samples of boundary points in a single trial, where (a) is from YOLO111-seg (Trial 1 in Tab. IV) and (b) is from DT2-seg (Trial 2).

indicate that the dissection process did not significantly alter the boundary, even though boundary updates were performed in real-time. This validates the effectiveness of our grasping strategy in maintaining boundary stability during dissection, which was a key limitation in our previous study. We fitted a cubic spline to the recorded boundary points to quantify boundary consistency, computing the residual mean squared error (RMSE) between the points and the fitted curve, as shown in Table IV. Since the boundary points were fixed in our previous work, we excluded those results from the table. Additionally, we measured the total travel distance of the PCH during dissection and the time required to complete one full boundary dissection, including data from our prior study.

Model (Seg. + Kpt.)	Trial	RMSE (mm)	Distance (mm)	Duration (s)
DT2-seg +	1	-	60.3	104
	2	-	51.3	117
	3	-	28.7	79
DT2-kpt (Old)	4	-	36.3	92
	5	-	38.3	97
	6	-	45.5	116
Mean		-	43.4	100.8
Std. Dev.		-	11.3	14.6
DT2-seg + DT2-kpt (New)	1	0.42	50.5	29
	2	0.78	51.1	28
	3	0.50	65.2	35
	4	0.43	54.3	30
	5	0.46	82.9	40
Mean		0.51	60.8	32.4
Std. Dev.		0.13	13.7	5.3
MaskDINO + YOLO111-pose	1	0.51	56.1	60
	2	0.63	46.3	30
	3	0.53	65.5	59
	4	0.49	69.3	64
	5	0.49	62.3	65
Mean		0.53	59.9	55.4
Std. Dev.		0.05	9.0	14.5
YOLO111-seg + YOLO111-pose	1	0.47	54.9	31
	2	0.52	47.2	29
	3	0.47	56.0	32
	4	0.50	54.9	31
	5	0.51	48.0	29
Mean		0.49	52.2	30.6
Std. Dev.		0.02	4.2	1.3

TABLE IV: Performance metrics across different models (Seg. + Kpt.) and trials. Residual mean squared error (RMSE) of the boundaries (Fig. 8) and the average and standard deviation values across trials are provided in the last row for each model.

As shown in Table IV, the YOLO11 model achieved the lowest RMSE, maintaining consistency across trials. In con-

trast, other models exhibited occasional RMSE spikes even though we removed the outliers for DT2-seg and MaskDINO before the analysis. A similar trend was observed for the travel distance of the PCH, where YOLO11 demonstrated stable performance while other models experienced variability, shown by a higher variance in all measurements for DT2 and MaskDINO. These discrepancies can be attributed to the limited predictive accuracy of DT2-kpt (as illustrated in Fig. 6) and noise in the point clouds surrounding the instrument, which led to wrong instrument tip positions. This, in turn, caused oscillatory movements of the robotic arm, increasing both travel distance and the duration of the procedure.

Furthermore, the dissection speed significantly improved compared to our previous DT2 (Old) and current DT2 (New) results. This improvement can be attributed to two main factors. First, the updated DT2-kpt model, trained on a more recent dataset, provided more accurate instrument keypoint predictions than the outdated version used in previous work. Second, the alignment of the PCH being orthogonal to the gallbladder surface before dissection minimized contact between the PCH and the liver, preventing the instrument from getting stuck at specific locations.

V. CONCLUSION

In this work, we presented a comprehensive framework for automated robotic dissection in cholecystectomy. Building on our previous efforts, we introduced a novel segmentation dataset derived from a more realistic robotic cholecystectomy dataset (CRCD). Additionally, incorporating the liver bed class improved boundary tracking even after cauterization. We fine-tuned state-of-the-art instance segmentation models, including MaskDINO and YOLO11, and compared their performance with our previously used model, Detectron2.

Furthermore, we transitioned from offline to online boundary point extraction, improving the methodology to ensure robustness under challenging surgical conditions, including multiple dissections, tissue color changes over time, and gallbladder size and shape variations. Additionally, we aligned the surgical instruments to the gallbladder surface before each action, enhancing task performance. We also introduced an automated bimanual manipulation strategy that integrates grasping and pulling actions, which are crucial for maintaining optimal tissue tension and compensating for shifts caused by energy application. To validate our framework, we conducted ex-vivo evaluations on porcine livers, demonstrating improved surgical instrument localization and precise dissection, even after the tissue deformation.

While this extended framework improved upon our previous work and addressed key limitations, further refinements are necessary. Through our work with the CRCD, we observed that surgeons employ different dissection techniques. One approach, as implemented in our current framework, involves following the boundary after stretching the boundary between the gallbladder and liver. However, another common technique involves using the tip of the PCH to hook the boundary and either pulling until the tissues detach

or applying energy if the tissue remains too thick after pulling. This method minimizes damage to the liver during energy application, reducing the risk of severe postoperative complications [31].

Hence, future work will focus on adding these different dissection techniques to our framework. Although the key-point detection has improved from our previous work, it still suffered in certain poses or situations during the task. So we plan to further augment the dataset for the keypoints using the CRCDD dataset, similar to how we expanded the segmentation dataset. We also aim to refine our control strategy to fully separate the gallbladder from the liver, accomplishing multiple rounds of pulling and dissecting the gallbladder autonomously and comparing the performance with the surgeons.

Overall, our contributions mark a significant advancement in robotic-assisted surgery, providing a robust foundation for the future development of autonomous dissection techniques in minimally invasive procedures.

REFERENCES

- [1] E. Ayvali, R. A. Srivatsan, L. Wang, R. Roy, N. Simaan, and H. Choset, "Using bayesian optimization to guide probing of a flexible environment for simultaneous registration and stiffness mapping," in *2016 IEEE International Conference on Robotics and Automation (ICRA)*. IEEE, 2016, pp. 931–936.
- [2] A. Shademan, R. S. Decker, J. D. Opfermann, S. Leonard, A. Krieger, and P. C. W. Kim, "Supervised autonomous robotic soft tissue surgery," *Science Translational Medicine*, vol. 8, no. 337, pp. 337ra64–337ra64, 2016. [Online]. Available: <https://www.science.org/doi/abs/10.1126/scitranslmed.aad9398>
- [3] D. Á. Nagy, T. D. Nagy, R. Elek, I. J. Rudas, and T. Haidegger, "Ontology-based surgical subtask automation, automating blunt dissection," *Journal of Medical Robotics Research*, vol. 3, no. 03n04, p. 1841005, 2018.
- [4] R. Jackson, V. Desai, J. Castillo, and M. Çavuşoğlu, "Needle-tissue interaction force state estimation for robotic surgical suturing," *Rep U S*, vol. 2016, pp. 3659–3664, Oct 2016, PMID: 29214097; PMCID: PMC5713916.
- [5] B. Lu, B. Li, W. Chen, Y. Jin, Z. Zhao, Q. Dou, P.-A. Heng, and Y. Liu, "Toward image-guided automated suture grasping under complex environments: A learning-enabled and optimization-based holistic framework," *IEEE Transactions on Automation Science and Engineering*, vol. 19, no. 4, pp. 3794–3808, 2022.
- [6] S. Iyer, T. Looi, and J. Drake, "A single arm, single camera system for automated suturing," in *2013 IEEE International Conference on Robotics and Automation*. IEEE, 2013, pp. 239–244.
- [7] S. Sen, A. Garg, D. V. Gealy, S. McKinley, Y. Jen, and K. Goldberg, "Automating multi-throw multilateral surgical suturing with a mechanical needle guide and sequential convex optimization," in *2016 IEEE International Conference on Robotics and Automation (ICRA)*, 2016, pp. 4178–4185.
- [8] R. Jackson, R. Yuan, D. Chow, W. Newman, and M. Çavuşoğlu, "Real-time visual tracking of dynamic surgical suture threads," *IEEE Trans Autom Sci Eng*, vol. 15, no. 3, pp. 1078–1090, Jul 2018, epub 2017 Aug 11. PMID: 29988978; PMCID: PMC6034738.
- [9] B. T. Ostrander, D. Massillon, L. Meller, Z.-Y. Chiu, M. Yip, and R. K. Orosco, "The current state of autonomous suturing: a systematic review," *Surgical Endoscopy*, vol. 38, no. 5, pp. 2383–2397, 2024.
- [10] A. Sagitov, T. Tsoy, H. Li, and E. Magid, "Automated open wound suturing: detection and planning algorithm," *Journal of Robotics, Networking and Artificial Life*, vol. 5, pp. 144–148, 2018. [Online]. Available: <https://doi.org/10.2991/jrnal.2018.5.2.16>
- [11] C. Gao, X. Liu, M. Peven, M. Unberath, and A. Reiter, "Learning to see forces: Surgical force prediction with rgb-point cloud temporal convolutional networks," in *OR 2.0 Context-Aware Operating Theaters, Computer Assisted Robotic Endoscopy, Clinical Image-Based Procedures, and Skin Image Analysis: First International Workshop, OR 2.0 2018, 5th International Workshop, CARE 2018, 7th International Workshop, CLIP 2018, Third International Workshop, ISIC 2018, Held in Conjunction with MICCAI 2018, Granada, Spain, September 16 and 20, 2018, Proceedings 5*. Springer, 2018, pp. 118–127.
- [12] M. Pan, K. Wang, G. Du, C. Ma, M. Li, and K. Liang, "A review of image-based force estimation," *Available at SSRN 5115117*.
- [13] S. Lu, Y. Luo, D. Xie, W. Wang, W. Zheng, and J. Gong, "Spatial mapping method of craniostylosis surgical robot based on point cloud registration," in *2021 6th Asia-Pacific Conference on Intelligent Robot Systems (ACIRS)*. IEEE, 2021, pp. 1–6.
- [14] T. D. Nagy and T. Haidegger, "A dvrk-based framework for surgical subtask automation," *Acta Polytechnica Hungarica*, pp. 61–78, 2019.
- [15] C. Molnár, T. D. Nagy, R. N. Elek, and T. Haidegger, "Visual servoing-based camera control for the da vinci surgical system," in *2020 IEEE 18th International Symposium on Intelligent Systems and Informatics (SISY)*, 2020, pp. 107–112.
- [16] R. Chiranjeevi, S. Jaganmohan, V. Thomas *et al.*, "Intelligent auto annotation system for identifying vehicles without number plates using grounding dino and segment anything model," in *2024 Second International Conference on Advances in Information Technology (ICAIT)*, vol. 1. IEEE, 2024, pp. 1–5.
- [17] C. D'Ettore, A. Stilli, G. Dwyer, M. Tran, and D. Stoyanov, "Autonomous pick-and-place using the dvrk," *International Journal of Computer Assisted Radiology and Surgery*, vol. 16, no. 7, pp. 1141–1149, 2021.
- [18] K.-H. Oh, L. Borgioli, M. Žefran, L. Chen, and P. C. Giulianotti, "A framework for automated dissection along tissue boundary," in *2024 10th IEEE RAS/EMBS International Conference for Biomedical Robotics and Biomechanics (BioRob)*. IEEE, 2024, pp. 1427–1433.
- [19] K.-H. Oh, L. Borgioli, A. Mangano, V. Valle, M. Di Pangrazio, F. Toti, G. Pozza, L. Ambrosini, A. Ducas, M. Žefran, L. Chen, and P. C. Giulianotti, "Comprehensive robotic cholecystectomy dataset (crcdd): Integrating kinematics, pedal signals, and endoscopic videos," in *2024 International Symposium on Medical Robotics (ISMR)*, 2024, pp. 1–7.
- [20] K.-H. Oh, L. Borgioli, A. Mangano, V. Valle, M. Di Pangrazio, F. Toti, G. Pozza, L. Ambrosini, A. Ducas, M. Žefran *et al.*, "Expanded comprehensive robotic cholecystectomy dataset (crcdd)," *arXiv preprint arXiv:2412.12238*, 2024.
- [21] F. Li, H. Zhang, H. xu, S. Liu, L. Zhang, L. M. Ni, and H.-Y. Shum, "Mask dino: Towards a unified transformer-based framework for object detection and segmentation," 2022.
- [22] G. Jocher and J. Qiu, "Ultralytics yolo11," 2024. [Online]. Available: <https://github.com/ultralytics/ultralytics>
- [23] Y. Wu, A. Kirillov, F. Massa, W.-Y. Lo, and R. Girshick, "Detectron2," <https://github.com/facebookresearch/detectron2>, 2019.
- [24] N. Ravi, V. Gabeur, Y.-T. Hu, R. Hu, C. Ryal, T. Ma, H. Khedr, R. Rädle, C. Rolland, L. Gustafson *et al.*, "Sam 2: Segment anything in images and videos," *arXiv preprint arXiv:2408.00714*, 2024.
- [25] J. Brooks, "COCO Annotator," <https://github.com/jsbrooks/coco-annotator/>, 2019.
- [26] T.-Y. Lin, M. Maire, S. Belongie, L. Bourdev, R. Girshick, J. Hays, P.-Y. Perona, D. Ramanan, C. L. Zitnick, and P. Dollár, "Microsoft coco: Common objects in context," 2014. [Online]. Available: <https://arxiv.org/abs/1405.0312>
- [27] P. Kazanzides, Z. Chen, A. Deguet, G. S. Fischer, R. H. Taylor, and S. P. DiMaio, "An open-source research kit for the da vinci surgical system," in *IEEE Intl. Conf. on Robotics and Auto. (ICRA)*, Hong Kong, China, 2014, pp. 6434–6439.
- [28] S. Macenski, T. Foote, B. Gerkey, C. Lalancette, and W. Woodall, "Robot operating system 2: Design, architecture, and uses in the wild," *Science Robotics*, vol. 7, no. 66, p. eabm6074, 2022. [Online]. Available: <https://www.science.org/doi/abs/10.1126/scirobotics.abm6074>
- [29] T.-C. Lee, R. L. Kashyap, and C.-N. Chu, "Building skeleton models via 3-d medial surface axis thinning algorithms," *CVGIP: graphical models and image processing*, vol. 56, no. 6, pp. 462–478, 1994.
- [30] H. Abdi and L. J. Williams, "Principal component analysis," *Wiley interdisciplinary reviews: computational statistics*, vol. 2, no. 4, pp. 433–459, 2010.
- [31] S. Jaunoo, S. Mohandas, and L. Almond, "Postcholecystectomy syndrome (pcs)," *International Journal of Surgery*, vol. 8, no. 1, pp. 15–17, 2010. [Online]. Available: <https://www.sciencedirect.com/science/article/pii/S1743919109001538>